

# The Effect of Graphene Ultrasonic Coating on Recycled Rubber

Maria Rosaria Marsico,\* Julián Mauricio Londoño Monsalve, Li Lu, and Monica F. Craciun

Herein, the mechanical behavior of a graphene-recycled rubber compound is investigated by performing static and dynamic tests. Water-based graphene suspension is deposited on recycled rubber pads via an electrostatic addition process. Results on tensile and compression tests indicate a significant improvement of the compound in strength and in damping. They also indicate that the compound experiences significant elongation (up to 500%) as well as withstands high tensile forces, 300% greater than the force that the recycled rubber mix would withstand. The effective compression modulus of the compound is also shown to increase by about 3.2 times at 10% strain with respect to the one for the recycled rubber mix. Results suggest that the graphene-recycled rubber compound can deliver a sustainable solution for vibration mitigation applications.

## 1. Introduction

Steel-reinforced elastomeric isolators, known as SREI, are structural bearings used to mitigate ground-borne vibrations. They are interposed between the structure and its foundations to decouple them, for instance, they are used in buildings to mitigate vibrations from earthquakes and train-induced vibrations. SREI are also one of the key components of bridges as they allow natural movements caused by thermal expansion, contraction, creep, shrinkage, or fatigue, without creating harmful stress on the bridge. Typically, they are made with natural rubber (NR) alternate with steel shims; the reinforcing steel shims constrain the rubber layers from lateral expansion and provide high vertical stiffness but have no effect on the shear stiffness.<sup>[1,2]</sup> Manufacturing SREI involves vulcanization to secure the bonding between the elastomer and steel shims and to add end steel

plates at the top and bottom to be attached to the structure by mechanical fasteners.<sup>[3]</sup>

In the past decade, researchers have investigated the use of fibers (e.g., carbon or glass) to reinforce the elastomer with the intent to reduce their weight therefore their manufacturing and transportation costs.<sup>[4]</sup> They have also investigated cold vulcanization processes to replace the traditional hot vulcanization using a bonding agent between rubber and fibers and they suggest taking off the end steel plates to further lighten them. Scaled models of unbounded fiber-reinforced elastomeric isolators (U-FREI) have been also tested experimentally and numerical models have been proposed. U-FREI show a reduction of

the stress in the device compared with SREI. Under horizontal excitations, the unanchored device rolls off and this reduces the high tensile stress region that would develop if the bearings were bonded,<sup>[5]</sup> but it shows dependence on fiber alignments and preloading history.<sup>[6,7]</sup>


Stratton et al.<sup>[8]</sup> conducted an experimental program to evaluate the effect of lateral coupling in rectangular unbonded fiber-reinforced elastomeric isolators and they found to exhibit lateral coupling but the degree of coupling and the impact on the structural performance under bidirectional loading is yet under investigation. They also derived a theoretical model to calculate the lateral stiffness based on the angle of loading and lateral displacement.

U-FREI have been studied in various configurations. Van Engelen et al.<sup>[9]</sup> conducted an initial experimental investigation on unbonded fiber-reinforced elastomeric isolators with modified support geometry. The aim of the study was to increase the efficiency of the isolator and protect the system against extreme displacements in events that meet or exceed the maximum considered event. They use modified support geometry to extend the softening regime and lower the effective horizontal stiffness, therefore, resulting in a larger shift in the fundamental period of the structure.

Castillo Ruano and Strauss<sup>[4]</sup> study the numerical model of unbonded fiber-reinforced elastomeric isolators by introducing a numerical material model for the elastomer matrix to capture the nonlinear hysteretic behavior of the devices. They also discuss the pronounced effect of the orientation of the reinforcement on large horizontal deformations, especially after the occurrence of a full rollover.

International codes are yet conservative; they state that an isolator shall consist of alternate layers of elastomer and steel and

M. R. Marsico, J. M. Londoño Monsalve, L. Lu, M. F. Craciun  
College of Engineering  
Mathematics and Physical Sciences  
University of Exeter  
Exeter EX4 4QF, UK  
E-mail: m.r.marsico@exeter.ac.uk

 The ORCID identification number(s) for the author(s) of this article can be found under <https://doi.org/10.1002/adem.202200957>.

© 2022 The Authors. Advanced Engineering Materials published by Wiley-VCH GmbH. This is an open access article under the terms of the Creative Commons Attribution License, which permits use, distribution and reproduction in any medium, provided the original work is properly cited.

DOI: 10.1002/adem.202200957

that for the elastomer virgin material shall be used and two thick end plates shall be hot bonded.<sup>[3]</sup>

High damping rubber bearings (HDRB) are widely employed for seismic isolation applications<sup>[10,11]</sup> due to higher damping capacity and higher capacity of supporting large loads compared with NR bearings.<sup>[12]</sup> They are made with alternative layers of steel shims and rubber and are secured to structure and foundations with end steel plates. The rubber is filled with particles, carbon black, oils, or resins to provide energy dissipation capacity. Their nonlinear behavior, that is high stiffness and damping at low shear strains and low shear stiffness at the design displacement level, and an increase in stiffness and damping at higher displacement, is very attractive. However, the bilinear idealizations used to simplify the analysis and overcome the highly nonlinear behavior may be inadequate in some applications for instance in tall buildings experiencing tensions.<sup>[13]</sup>

NR filled with graphene nanosheets dispersed in the rubber matrix has been studied in other studies<sup>[14,15]</sup> to demonstrate toughening and crack improvement. The nanocomposite was studied under tensile loading and unloading cycles and it was shown that the graphene filler has a remarkable effect on increasing the energy dissipation and the crack resistance of the composite.

Likewise, the performance of nanocomposites prepared by the conventional two-roll mill mixing of NR and functionalized graphene sheets is studied in the study by Hernandez et al.<sup>[16]</sup> Results show an increase in the electrical conductivity and enhancement in the mechanical behavior due to strong rubber-to-filler interactions. Graphene oxide (GO) is also considered as an ideal rubber nanofiller due to its easy preparation, plentiful oxygen groups, and large surface area, and it is shown to exhibit high reinforcing efficiencies for styrene-butadiene rubber; however, the compatibility of GO with nonpolar rubber is poor and homogeneous dispersion of graphene in rubber-like materials remains still demanding.<sup>[17]</sup>

Marsico et al.<sup>[18]</sup> conducted an experimental frequency response study on NR pads reinforced with layers of graphene. To transfer graphene films on rubber pads, the isopropyl alcohol-assisted direct transfer method developed by the authors is used.<sup>[19]</sup> Their results show that few-layer graphene transferred on a rubber pad increases stiffness and damping of the graphene-based composite; also, they show that the mechanical properties of the graphene-rubber composite alter when varying the thickness of few-layer graphene transferred on rubber pads.

The use of alternative materials for SREI remains essential not only for reducing the cost of the devices due to the long, bespoke manufacturing process but also to reduce the environmental impact elastomeric isolators might have due to employing virgin materials to comply with the standards.

In this article, we explore alternative methods to facilitate the scalability of the process to deposit graphene. We use ultrasonic spray coating, which is employed in various emerging applications, including solar cells,<sup>[20,21]</sup> organic light-emitting devices,<sup>[22]</sup> and electrodes<sup>[23,24]</sup> and it proved to be a viable technique allowing rapid deposition of large surfaces with nanoparticles.<sup>[25]</sup>

This article presents an experimental investigation on recycled rubber coated with different types of graphene and different coating layers. The samples were made using 50% recycled rubber

from tires and 50% NR. An ultrasonic spray-coating machine is used to deposit graphene layers on rubber pads. Static and quasistatic tests were performed, and the mechanical properties of the samples are derived. Results show that the graphene coat enhances the mechanical behavior of the rubber pads, envisaging applications of the graphene-recycled rubber compound for vibration isolation of structures.

## 2. Graphene Deposition

Graphene suspensions were prepared by dispersing commercial graphene nanoplatelets (GNP) powder in deionized water using a high-shear laboratory mixer (capacity from 1 mL up to 12 L and the ability to mix in-line with flow rates up to 20 L min<sup>-1</sup>) with a 32 mm-diameter rotor head. The concentration of the graphene suspension is 1.5 g l<sup>-1</sup> and exfoliated at 5000 rpm for 3 h.

Two types of GNPs were used, namely, Elicarb products from Thomas Swan Ltd (TS: carbon 90%, oxygen 9%; Na<1%) and GNPs from Cheap Tubes (CT: purity >97% water, diameter 2 μm, Grade 3). CT water-based graphene suspension is black and stable without settling of graphene flakes for at least several hours, whereas TS graphene suspension is light gray and can be settled in water within 2 h. The graphene suspension can be kept at room temperature for months without quality fluctuation.

The deposition of graphene films on the recycled rubber pads was performed using an automated programmable benchtop ultrasonic coating system with a 300 mm × 300 mm work area. The hotplate temperature for the spray is set at 120 °C as the suspension is water based. The spray coater is equipped with an ultrasonic nozzle, which offers unique benefits when spraying nanoparticles in suspension, keeping them evenly suspended during the entire spray process through the ultrasonic action of the nozzle itself. Specifically, the ultrasonic nozzle converts high-frequency sound waves into mechanical energy that is transferred into the GNP water suspension, which is fed through the center of the nozzle. As the suspension exits the atomizing surface of the nozzle, it bursts into a fine mist of uniform micrometer-sized droplets. Low-pressure air (6.5 bar) was used to precisely shape atomized spray into defined patterns for uniform high-throughput wide-area coating of graphene on the rubber pads. A low flow rate of 0.7 mL min<sup>-1</sup> allows water to be evaporated sufficiently while promoting the graphene flakes interacting with the rubber surface. This results in more uniform dispersion of functional particles in thinner layers. The number of cycles that is the travel time between one edge to the other edge of the spray area was varied to optimize the thickness of the deposited film.

## 3. Experimental Tests

To assess the effect of graphene on a recycled rubber mix, we conducted tensile and compression tests on specimens coated with different cycles of graphene deposition, where each cycle is the return travel route of the nozzle.

For tensile tests, we used an Instron universal testing machine with a 30 kN load capacity loadcell. Tests were conducted at standard ambient temperature (23 ± 2 °C) according to other studies,<sup>[26,27]</sup> on die-cut C dogbone specimens clamped into the

**Table 1.** Dogbone specimens' geometry for tensile test.

Set	Specimen	Width [mm]	Thickness [mm]	Gauge length [mm]
5	5R	0.973	1.93	80
	5G	0.986	2.17	80
6	6R	4.92	3.21	30
	6G	5.08	3.44	30

grips and we pulled the grips apart at a speed of  $10 \text{ mm min}^{-1}$  until the specimen broke; thickness and width of the specimens were measured three times, with the median value being the accepted value as recommended by standards. We tested two sets of specimens, namely, sets 5 and 6. For set 5 we tested specimens 5R (regular) and 5G (graphene), with an overall length of 146 mm (gauge length 80 mm) and made with 50% recycled and 50% virgin rubber. Specimen 5R had an average thickness of 1.93 mm and an average width of 0.973 mm. On specimen 5G we deposited 200 cycles of CT graphene, the specimen had an average thickness of 2.17 mm and an average width of 0.986 mm.

For set 6 we tested specimens 6R and 6G with an overall length of 80 mm (gauge length 30 mm) and made with 50% recycled and 50% virgin rubber (rubber composition is the same as set 5). Specimen 6R had an average thickness of 3.21 mm and an average width of 4.92 mm. On specimen 6G, we deposited 200 cycles of CT graphene, the specimen had an average thickness of 3.44 mm and an average width of 5.08 mm. **Table 1** summarizes the specimens' geometry and average width and thickness.

Experimental results show that 200 cycles of CT graphene deposited on the rubber substrate result in a significant increase in the specimens' stiffness. For instance, for a 100 mm elongation, the stiffness of specimen 5G (6R) is 3.8 (3.5) greater than the stiffness of specimen 5R (6R), where the stiffness  $K$  is given by

$$K = F/\delta \quad (1)$$

with  $F$  the tensile force and  $\delta$  the elongation. **Figure 1** shows the force–elongation curves from tensile tests on set 5 and set 6 specimens.

Pressed sheets of recycled rubber mix were used to die cut dogbone specimens. The thickness of the sheets was variable; therefore, stress–strain plots were generated to make results from different specimens comparable. If we define the strain  $\varepsilon$  as

$$\varepsilon = \Delta_L/L_0 \quad (2)$$

where  $\Delta_L$  is the difference between the final elongation and the initial length of the gauge and  $L_0$  is the initial length of the gauge (146 mm for set 5 and 80 mm for set 6), and the stress ( $\sigma$ ) as the ratio between the force  $F$  that attempts to stretch the specimen and the cross-sectional area of the specimen  $A$ , we can plot the stress–strain ( $\sigma$ – $\varepsilon$ ) curve. For set 5 the maximum strain before the breaking point reduces to about 31% in specimen 5G compared with specimen 5R, whereas for set 6 the variation in strain is dismissible (3% reduction in a strain of specimen 6G compared with specimen 6R). Stress at the breaking point of specimens reinforced with graphene, 5G and 6G, increases, respectively, by about 300% and 340% with respect to the stress in specimens 5R and 6R. **Figure 2** shows the stress–strain ( $\sigma$ – $\varepsilon$ ) curves of the four specimens and it suggests that the rubber mixture does not experience crystallization, that is when the stress–strain curve steepens markedly, and the ultimate failure strength increases.<sup>[28,29]</sup>

Tensile stiffness of 5G specimens ( $0.46 \text{ N mm}^{-1}$ ) at 50 mm elongation is also shown to increase of about 4.3 times with respect to specimens 5R ( $0.11 \text{ N mm}^{-1}$ ) and it increases 5 times at 150 mm elongation; this would also be beneficial to the rubber mix to enhance its tensile strength.

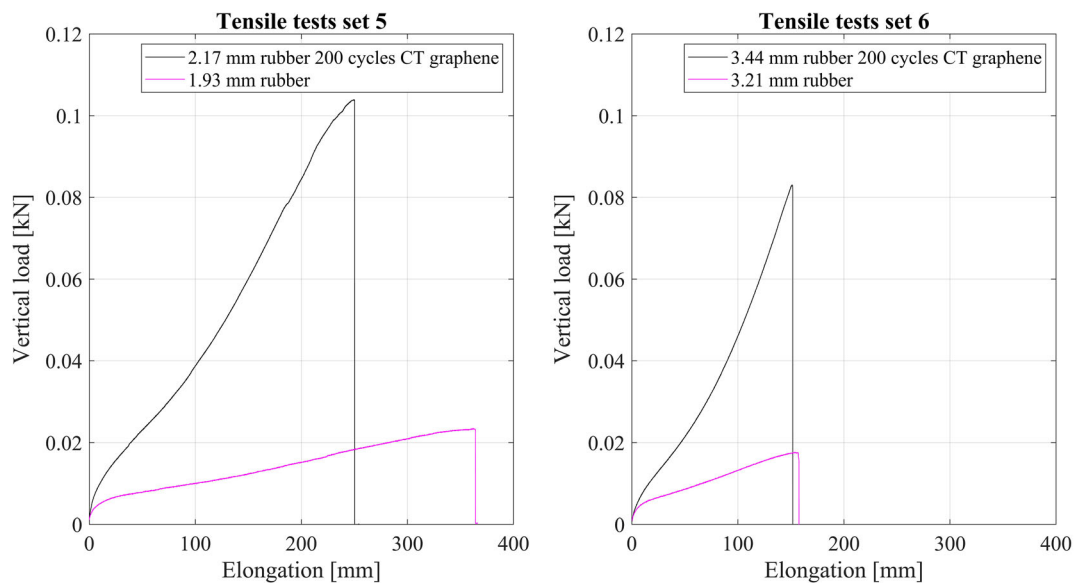


**Figure 1.** Force–elongation curves for set 5 with 146 mm length of gauge (left) and set 6 with 80 mm length of gauge (right). The thickness of the specimens is shown in the legend.

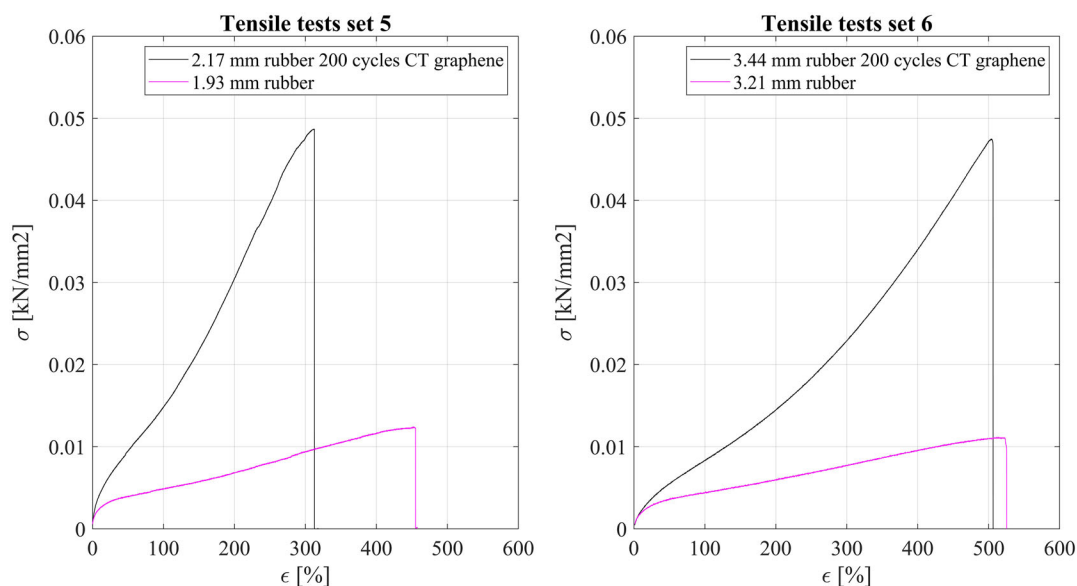


**Figure 2.** Stress–strain curves for set 5 with 146 mm length of gauge (left) and set 6 with 80 mm length of gauge (right).

The four specimens show a nonlinear behavior; the modulus value defined as the stress measurement made at a specified percentage of elongation is not constant but varies with the specimen's elongation.<sup>[30]</sup> This behavior, combined with the increase of stiffness, confirms that specimens 5G and 6G (with layered graphene) are less ductile than specimens 5R and 6R although experiencing significant increase of ultimate tensile strength. The latter, that is the maximum force the specimen can withstand without fracturing when stretched, is 12 MPa for specimens 5R and 6R and is 48 MPa for specimens 5G and 6G, that is  $\approx 300\%$  greater.

Modulus 10 (M10), M100, and M300 for sets 5 and 6 are summarized in Table 2, also showing the change of moduli in the percentage of the graphene-coated sample with respect to the regular specimens. They indicate the stress needed to stretch the rubber at the specific elongation of 10%, 100%, and 300%, respectively, and are a measure of the material stiffness in tension. It is evident that the addition of graphene layers on rubber

pads results in an increase of stiffness in tension, of about 400% in set 5 and 200% in set 6 specimens. Although the variation of moduli in graphene-coated and uncoated samples in set 6 is less marked than in set 5, the rate of the moduli change with elongation in set 6 specimens is higher than that in set 5 (from M10 to M300, M increases 12 times in set 6 and 5.6 times in set 5). A behaviour like the one experienced by set 6 specimens is desirable in applications that require a significant change in elongation (up to 500%) as well as withstanding high tensile forces (300% greater than the force that the mixed rubber would withstand).

#### 4. An Observation on the Hardness of the 50% Recycled–50% Natural Rubber Mix

The recycled rubber manufacturer has provided the hardness, defined as the resistance to indentation, of the 50% recycled–50% NR mix IRHD 65.8 (International Rubber Hardness) used in this study.<sup>[31]</sup> The provided IRHD sits within the range 45–75 A of typical values for rubber commonly used in engineered components and in elastomeric-bearing applications, and it suggests that the rubber mix used in this study would be appropriate for these applications.<sup>[32,33]</sup>

Researchers have developed a relationship between hardness and Young's modulus.<sup>[34–37]</sup> At very low strain, the stress–strain ratio defined as Young's modulus  $E$  in other studies<sup>[30,34]</sup> can be obtained from the almost-linear region where Hook's law is valid, and it is approximately the same whether the strain is applied in tension and in compression.<sup>[30]</sup> Lindley<sup>[34]</sup> collected values of hardness (above 30 IRHD and subjected to uncertainty of  $\pm 2$  degrees) and elastic moduli, based on experiments for typical NR spring vulcanizates. For hardness value IRHD 65 of NR containing semireinforcing furnace black as filler, close to IRHD 65.8 mix used for sets 5 and 6, Lindley suggests

**Table 2.** Tensile moduli of the four specimens at a specific elongation of 10%, 100%, 300%, and variation in percentage.

Set	Specimen	M10 [kN mm <sup>-2</sup> ]	M100 [kN mm <sup>-2</sup> ]	M300 [kN mm <sup>-2</sup> ]
5	5R	0.00248	0.00487	0.00947
	5G	0.00426	0.01489	0.04813
	Variation between 5R and 5G	72%	206%	408%
6	6R	0.00196	0.00455	0.00771
	6G	0.00228	0.00863	0.02299
	variation between 6R and 6G	16%	90%	198%

a corresponding modulus  $E = 5.85$  MPa, shear modulus  $G_s = 1.37$  MPa, and bulk modulus  $B = 1210$  MPa. It is also suggested that for NR the most accepted value by codes of practice for bulk modulus is  $B = 2000$  MPa and since elastomers are sensibly incompressible, that is, they deflect by changing shape rather than changing volume, Poisson's ratio is approximately  $\nu = 0.5$ .<sup>[30,38]</sup> Those values are based on experiments and according to Lindley, their accuracy is about  $\pm 15\%$  in compression and  $\pm 50\%$  in shear.

To estimate numerically Young's modulus within the linear region of the stress–strain curve knowing the IRHD of rubber, Gent (1958) derived a theoretical relationship between hardness and Young's modulus.<sup>[35]</sup> The relationship given in Equation (3) is valid for vulcanized or thermoplastic rubber and we employed it to assess whether it could be extended to the uncured recycled rubber mix that we used for the specimens.

$$E(\text{MPa}) = \frac{0.0981 (56 + 7.66s)}{0.137505 (254 - 2.54s)} \quad (3)$$

This relationship is valid for IRHD exceeding 40, where  $s$  is the Shore hardness and as per,<sup>[39]</sup> another study, for highly elastic rubbers, the scales of IRHD and the Shore A durometer are comparable. By implementing Equation (3), Young's Modulus  $E$  for a rubber 65.8 IRHD (that is for set 5 and set 6 specimens) would be 4.59 MPa.

BS 903 (1950)<sup>[36]</sup> suggests a relationship that accounts for departures at low values, that is for hardness values below 40.<sup>[37]</sup> Although this relationship is not relevant to the case study presented in this manuscript (IRHD 65.8 > 40), it is reported here to provide a comprehensive overview of the relationship between hardness and Young's modulus within the linear region of the stress–strain curve. The relationship in another study<sup>[36]</sup> is given by

$$H = 100 \operatorname{erf} (kE^{1/2}) \quad (4)$$

where  $k = 3.186 \times 10^{-4} \text{ Pa}^{-1/2}$  and erf is the error function. By implementing Equation (4), the value of Young's Modulus  $E$  for 65.8 IRHD would be 4.45 MPa, which is closer to the value derived from Equation (3). The values for  $E$  derived from Equation (3) and (4) are very close to each other. They are smaller than the one measured by Lindley for IRHD 65 ( $E = 5.85$  MPa) although the value of  $E$  estimated using Equation (4) matches the value measured by Lindley for IRHD 60 ( $E = 4.45$  MPa); this confirms the uncertainty of Lindley's values as reported in the study by Lindley et al.<sup>[34]</sup> From this initial analysis, it was noticed that Equation (3) and (4) provide moduli values of 4.59 and 4.45 MPa, respectively, which are very close to the experimentally measured modulus at 100% elongation of the 50% recycled–50% NR mix,  $E = 4.87$  MPa (5R) and  $E = 4.55$  MPa (6R) and ultimately might represent a reasonable estimation for a preliminary design (see Table 2 for comparison).

## 5. Effect of Graphene-Coating Cycles on Tensile Stiffness of Composite

For a qualitative analysis on the morphology of the graphene layers corresponding to different types of deposited graphene,

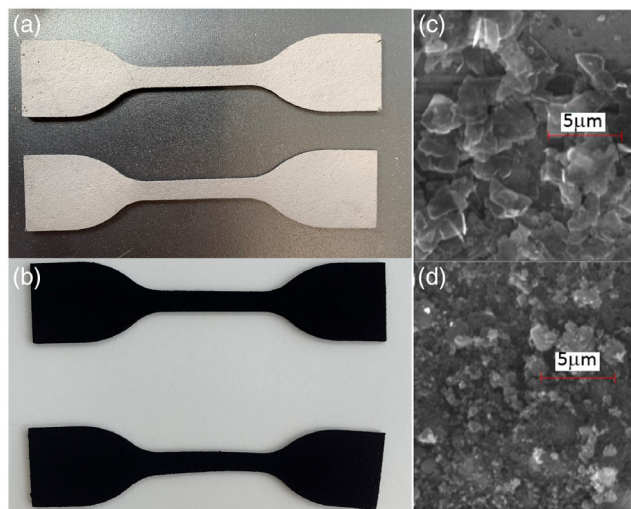


**Figure 3.** Dog bone Type A. a) Coated with TS graphene 58 and 90 cycles – light gray. b) Coated with CT graphene 110 and 200 cycles – black. c) SEM image of 58 cycles of TS graphene coated on Si. d) SEM image of 200 cycles of CT graphene coated on Si.

we have used a scanning electron microscope (SEM).<sup>[40]</sup> SEM observations were conducted on the different types of graphene layers deposited on a silicon substrate (Si) as this substrate is flatter than rubber and its size is more suitable for SEM; also the nonconductivity of rubber would require additional coating to make it conductive. **Figure 3** shows the SEM images for TS and CT types of graphene. Both types of graphene show nanoplatelets with an average size of  $7.504 \mu\text{m}^2$  for TS and  $0.926 \mu\text{m}^2$  for CT. We used an atomic force microscope for an initial estimate of the thickness for 20 and 140 cumulative cycles of CT graphene, resulting in a max of 80 nm and 2  $\mu\text{m}$ , respectively. This investigation has also provided some information about the relationship between the number of graphene cycles applied on the recycled rubber substrate and the thickness of the graphene layer, although further investigation is required to map this relationship factoring in the unevenness of the rubber substrate.

To gather more quantitative data, we conducted tensile tests on dogbone-shape specimens Type A ISO 37<sup>[26]</sup> with an overall length of 115 mm (gauge length 33 mm) and made with 50% recycled and 50% virgin rubber (same rubber composition as sets 5 and 6). The samples were coated with layers of graphene, that are 58 and 90 cycles for type TS graphene, and 110 and 200 cycles for type CT graphene, see **Figure 3**.

Results show that increasing the number of cycles of deposited graphene, the stiffness of the sample increases but not at the same rate as shown in **Figure 4**. The stress–strain curves shown in **Figure 4** (right) are comparable as experimental values are normalized with respect to the cross-sectional area of the gauge and the length of each sample. In particular, the stress–strain ratio at 300% elongation of the sample with CT 200 cycles is 5 times greater than the stress–strain ratio of the recycled rubber mix, and it is 4.8 times greater when the rubber is coated with 110 cycles of CT graphene. In contrast, from 58 cycles TS to 90 cycles TS graphene, the stress–strain ratio is respectively 1.3 and 2.4 times greater. This shows that the stress–strain ratio increases



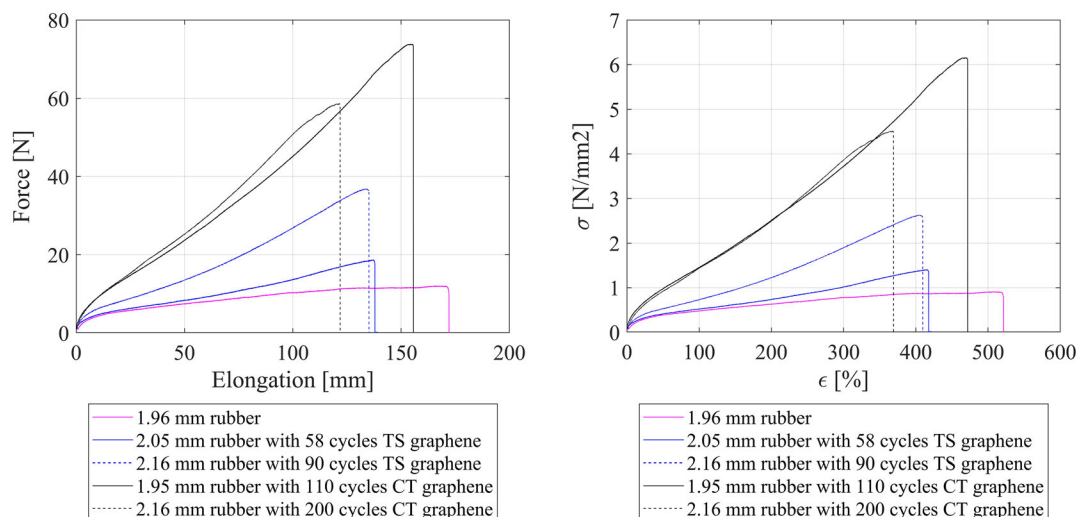


**Figure 4.** Tensile tests on rubber coated with various layers and types of graphene. Force–elongation curves (left); stress–strain curves (right).

faster when a few cycles of graphene are applied (from 58 to 90 cycles) and then the stress–strain ratio increases at a lower rate when additional cycles of graphene are added (from 110 to 200 cycles), foreseeing a plateau that would depend on the type of substrate and the penetration of graphene particles. **Figure 5** shows the relationship between the stress–strain ratio measured experimentally at maximum tensile strain and the number of cycles of graphene coating added on the specimens. The max stress–strain ratio appears to increase significantly in specimens coated with 60 cycles of graphene and to converge to almost the same value when 110 cycles of graphene are applied, showing that any further cycles of graphene coating wouldn't shift it. The effect of varying the GNP is under investigation. **Table 3** shows the stress–strain ratio of the tested specimens at 300% elongation. This result is extremely important in the assessment of the quantity of graphene needed to enhance the mechanical behavior of the rubber for the purpose of meeting the target mechanical properties.

**Table 3.** Stress–Strain ratio of five tested specimens at 300% elongation.

Stress–strain ratio at 300% elongation [ $\text{N mm}^{-2}$ ]	Sample composition
0.26	Rubber
0.34	Rubber with TS 58 cycles graphene
0.63	Rubber with TS 90 cycles graphene
1.24	Rubber with CT 110 cycles graphene
1.29	Rubber with CT 200 cycles graphene

## 6. Instantaneous Compression Modulus

Elastomeric isolators for vibrations isolation are typically made with alternate layers of rubber and steel shims. The steel shims constrain the global lateral bulging of the rubber to guarantee a

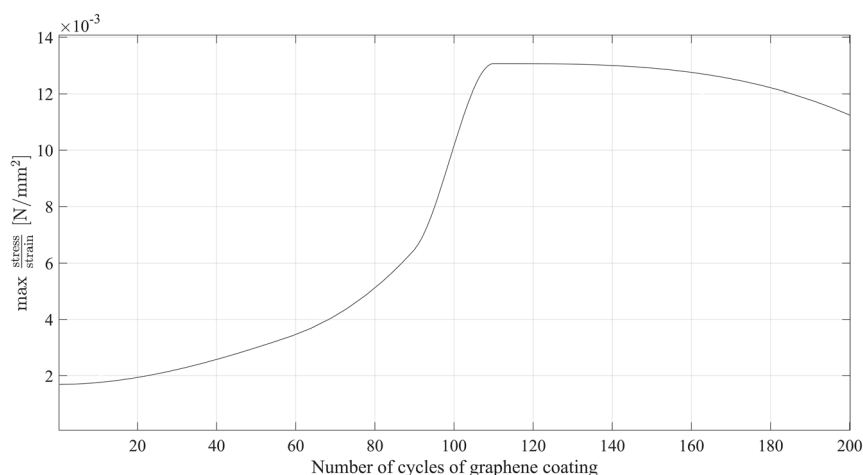


**Figure 5.** Relationship between the stress–strain ratio measured experimentally at maximum tensile strain and number of cycles of graphene coating.

**Table 4.** Experimental compression modulus of specimens uncoated, coated with 200 TS, and with 200 CT cycles graphene.

Set	Specimen	Width [mm]	Thickness [mm]	Length [mm]	Compression Modulus		
					at 10% [Mpa]	at 30% [Mpa]	at 50% [Mpa]
1	5R	21.7	1.66	22.3	4.19	17.06	24.30
2	TS	22.89	2.11	24.11	10.48	21.44	25.43
3	5G (CT)	22.99	2.06	22.53	13.42	23.15	28.71

certain vertical stiffness of the bearing.<sup>[41]</sup> The vertical stiffness of an elastomeric isolator depends on the instantaneous compression modulus  $E_c$  of an elastomer layer which has both sides provided with plates.  $E_c$  is estimated using the relationship proposed by<sup>[34,42]</sup>

$$E_c = E_0(1 + 2k'S) \quad (5)$$

where  $E_0$  is the compression modulus for unconfined rubber in a test machine for the stain of a few percent.  $E_0 = 3G_s$  for unfilled low-damping elastomers with effective damping ratio  $\xi_{\text{eff}} \leq 0.06$  at 100% shear strain, and  $E_0 = 4G_s$  for high-damping elastomers with carbon black filler with  $\xi_{\text{eff}} > 0.06$  at 100% shear strain,<sup>[3]</sup> where  $G_s$  is the shear modulus.  $S$  is the first shape factor, a dimensionless measure of the aspect ratio of the single layer of the elastomer and it is defined as the ratio between loaded area and force-free area. For a square specimen, the first shape factor  $S = a/(4t)$ <sup>[1]</sup> where  $a$  is the side of the square rubber pad (47 mm) and  $t$  is the layer thickness;  $k'$  is the material modifying factor determined experimentally and it is dependent on rubber hardness and for IRHD 65 Lindley measured  $k' = 0.54$ , while for IRHD 70  $k' = 0.53$ .<sup>[34]</sup>

One can measure  $E_0$  experimentally at various strain levels by performing compression tests on the virgin-recycled rubber mix coated and uncoated with graphene layers. Then the shape factor

of the tested specimens can be calculated, and the instantaneous compression moduli can be estimated using Equation (5).

We have conducted compression tests on three sets, each consisting of three identical specimens to enhance the reliability of results.<sup>[26]</sup> Set 1 consists of an uncured square pad made of 50% recycled and 50% virgin rubber (same composition as 5R specimen used for tensile tests). Set 2 is made by depositing 200 cycle TS graphene on same rubber compound as that used for set 1; similarly, set 3 is made by depositing 200 cycles of CT graphene on same rubber compound as that used for set 1. Samples' geometry is provided in Table 4. Thickness of the specimens has been measured using digital micrometers and measures have been taken at two edges and the middle of the square specimen and the average value was taken as per other studies.<sup>[26,27]</sup>

100-cycle tests were conducted at  $100 \text{ mm min}^{-1}$  and specimens were compressed up to 50% shortening. Stress-strain curves are shown in Figure 6 for the 10th, 50th, and last cycle. The first six cycles of loading-unloading are disregarded to contemplate the stress softening phenomenon.<sup>[43,44]</sup> Figure 6 also shows that coated specimens experience a loading-unloading behavior more stable than uncoated specimens. For instance, the stress in the 50th loading cycle with respect to the 10th loading cycle reduces by 0.003% in CT-coated specimens, by 0.0001% in TS-coated specimens, and by 0.005% in uncoated specimens. This foresees the durability of graphene coating under cyclic loadings.

Experimental compression moduli at 10%, 30%, and 50% stains for the 50th cycle of the dynamic tests are given in Table 4. They suggest that the experimental compression modulus of the rubber at 10% strain almost triples when the rubber is coated with graphene either TS or CT, whereas at 50% strain the compression moduli of the specimens with and without graphene are almost comparable. This result will inform the design of elastomeric devices for applications in which higher compression modulus and modest shortening are required, for example,

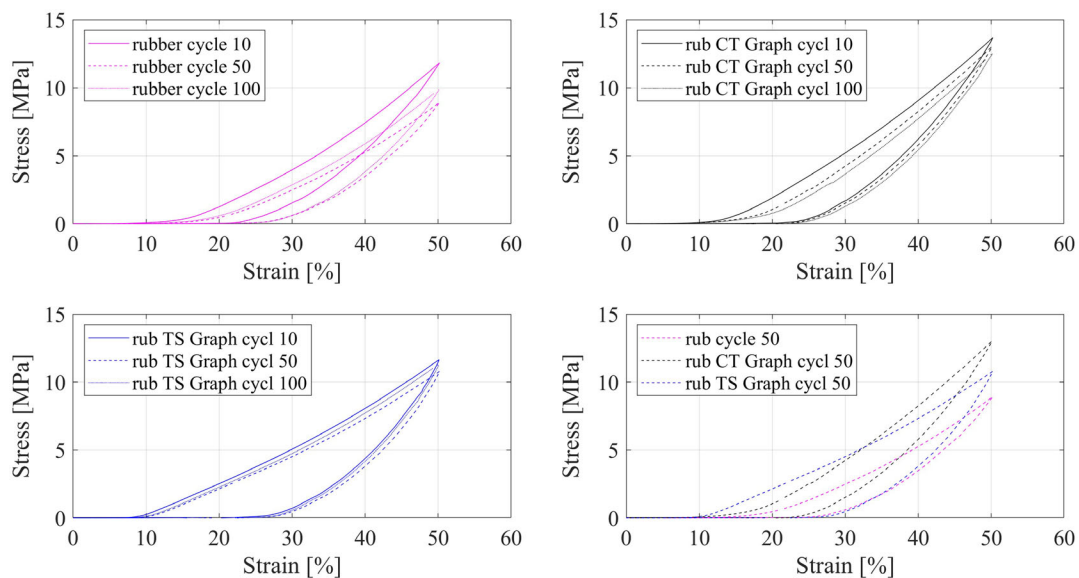


**Figure 6.** Stress-strain curves at 10th, 50th, and 100th cycle of the dynamic compression tests.

**Table 5.** Instantaneous compression modulus for specimens 5R and 5G at 10%, 20%, and 50% strain.

Set	Specimen	Strain	$E_0$ Compression modulus [MPa]	$k'$	Thickness [mm]	First Shape factor [S]	$E_c$ Instantaneous compression modules [MPa]		
5	5R	10%	4.19	0.53	1.66	7.08	35.61		
		30%	17.06				145.03		
		50%	24.30				206.59		
	5G	10%	13.42				2.06	5.70	94.54
		30%	23.15						163.15
		50%	28.71						202.32

in retrofitting buildings where the height of the room for housing the devices is predefined.

For a preliminary design, the stress–strain curves are assumed to be linear for strains up to 50%, therefore, the instantaneous compression moduli  $E_c$  have been estimated using Equation (5) and are given in **Table 5** at strains 10%, 20%, and 50%. If we assign to 5G the same first-shape factor of specimen 5R ( $S = 1.66$ ) and we name it specimen 5G<sub>M</sub> (Modified)—having the same geometry as 5G—we observe that  $E_c$  of specimen 5G<sub>M</sub> is 3.2 greater than  $E_c$  of specimen 5R at 10% strain and that the ratio  $E_c(5G_M)/E_c(5R)$  decreases when strain increases, from 3.2 at 10% to 2.1 at 50%. **Table 6** shows the instantaneous compression modulus for the modified specimen 5G<sub>M</sub> at different percentage strains.

## 7. Estimation of the Experimental Damping Ratio

Elastomeric isolators are used for seismic isolation and aim to shift the fundamental frequency of a structure away from the dominant frequencies of earthquake ground motion and the fundamental frequency of the fixed base superstructure. In addition to this, they should provide an additional means of energy dissipation, thereby reducing the transmitted acceleration into the superstructure.<sup>[45]</sup> To estimate the experimental damping ratio of the specimens, we employ the theory developed for equivalent damping of hysteresis damper in which the viscoelastic property of the damper is represented by Kelvin's model. We have conducted compression tests with maximum strain equal to 50% of the thickness of the sample, and we have used the area enclosed in the force–displacement hysteretic loop to estimate the energy dissipated in each cycle. The energy dissipated can be estimated as

$$\Delta_W = \pi K \beta x^2 \quad (6)$$

where  $x$  is the maximum deflection and  $K$  is the slope of the loop from the hysteretic loop. The structural or hysteretic damping coefficient  $\beta$  (also known as  $\eta$ ) is

$$\beta = (\Delta_W)/(\pi K x^2) \quad (7)$$

and the logarithmic decrement is

$$\delta = \pi \beta \quad (8)$$

Then, can estimate the damping ratio as

$$\xi = \beta/2 \quad (9)$$

The damping ratio  $\xi$  was estimated using Equation (9). For the rubber coated with TS graphene, the initial damping  $\xi$  at the first loading–unloading cycle is estimated at 0.042, whereas for the rubber coated with CT graphene,  $\xi = 0.035$  (both low damping according to.<sup>[3]</sup> Those values are, respectively, 68% and 42% greater than the damping ratio of the recycled rubber mix, estimated at 0.025 from compression tests. Compared with the damping for the mixed rubber ( $\xi = 0.0164$ ), the damping at the 50th cycle is 17% greater for the rubber coated with CT graphene and 107% greater for the rubber coated with TS graphene. Despite a decrease in damping with dynamic fatigue, the recycled rubber mix coated with graphene continues to be higher damped than the uncoated mix. This suggests that adding  $n$ -cycles graphene on rubber would increase damping into the system in such a way that it reaches an equivalent damping ratio for HDRB with a lead core. This would be beneficial for applications in bridges where HDRB or external dampers (e.g., viscous dampers in long-span suspension bridges) providing the required damping to the system wouldn't be needed anymore. It is worth noticing that despite promising initial results the characterization of the dynamic behavior of the material is not complete yet and further studies are required to ultimately explore applications in various industry sectors.

Results from compression tests also show that the compression stiffness of the rubber pad coated with graphene increases with respect to the compression stiffness of the uncoated rubber, in particular at the 50th cycle, the compression stiffness of set 3 specimens is 22% greater and of set 2 specimens is 10% greater than the one for set 1 specimens. This result also brings to light an important aspect of this study that is the effect of the composition of the deposited graphene on the mechanical behavior of the composite envisaging effect on the penetration and development of crosslink in the vulcanization process.<sup>[28]</sup> **Figure 7** shows the estimated damping and compression

**Table 6.** Instantaneous compression modulus for the modified specimen 5G<sub>M</sub> at 10%, 30%, and 50% strain.

Specimen	Strain	$E_0$ Compression modulus [MPa]	$k'$	Thickness [mm]	First Shape factor [S]	$E_c$ Instantaneous compression modules [MPa]	$E_c(5G_M)/E_c(5R)$
5G <sub>M</sub>	10%	13.42	0.53	1.66	7.08	114.09	3.20
	30%	23.15				196.88	1.36
	50%	28.71				244.15	1.18



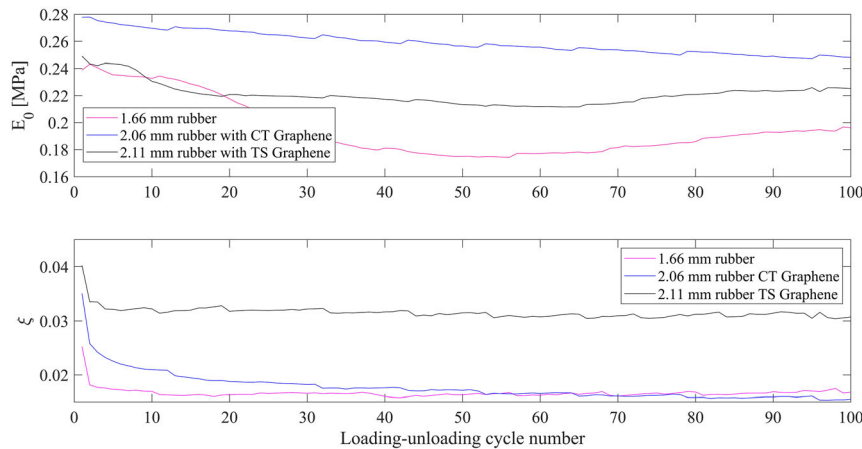


**Figure 7.** Compression modulus and damping are estimated at each compression loading–unloading cycle up to 100 hysteresis loops.

modulus at 50% shortening from hysteresis loops throughout 100 loading–unloading cycles.

## 8. Conclusion

This article presents an experimental investigation on recycled rubber pads coated with graphene. Different types of graphene have been deposited on rubber pads via electrostatic addition. We used the number of coating cycles as a proxy for the graphene thickness deposited on a 50% recycled–50% virgin rubber substrate. We are currently using different techniques to gather reliable measurements of graphene thickness and unevenness and results will be available to the scientific community soon as part of a dedicated study on graphene deposition on rubber. Results showed that the tensile stress–strain ratio increases significantly when a few cycles of graphene are applied on the recycled rubber substrate (from 58 to 110 cycles); the stress–strain ratio increases at a lower rate when additional cycles of graphene are added. A plateau effect for the stress–strain ratio appreciated at 300% elongation is under investigation, and it would depend on the type of composition of the recycled rubber mix and on the penetration of graphene particles in it.

Compression tests showed the desirable increase in vertical stiffness that would open the possibility of using graphene layers in lieu of steel shims to reinforce recycled rubber mix and use the recycled rubber–graphene composite in elastomeric devices for vibration mitigation. For these applications, the graphene film will not be exposed to environmental factors but embedded in two recycled rubber pads.

It has been observed that a few-layer graphene on recycled rubber increases the compression modulus and the damping in the recycled rubber–graphene compound. Moreover, we found evidence of a decay of compression modulus and damping due to fatigue effects, which are less pronounced in the coated recycled rubber than in the uncoated mix. This indicates that the graphene coating would enhance the durability of the recycled rubber, opening the possibility of using recycled rubber for elastomeric isolators. Likewise, the growth of damping in the coated recycled rubber would be beneficial for structural bearings as

they would not require the use of high damping rubber filled with particles or lead core to achieve the desired level of damping.

## Acknowledgements

M.R.M. and J.M.L.M. contributed equally to this work. The authors gratefully acknowledge the support of this research by the EPSRC Impact Acceleration Account 2021–2022.

## Conflict of Interest

The authors declare no conflict of interest.

## Author Contributions

M.R.M. conceived the project, designed the experiments, tested the specimens, and analyzed the results; J.M.L.M. designed and performed the experiments and analyzed the results. L.L. deposited graphene on rubber pads; M.F.C. provided the graphene samples and contributed to interpreting the results; M.R.M. and J.M.L.M. wrote the article with input from all authors.

## Data Availability Statement

The data that support the findings of this study are available from the corresponding author upon reasonable request.

## Keywords

damping, graphene spray coating, recycled rubber, vibration isolation

Received: June 30, 2022

Revised: August 22, 2022

Published online:

[1] J. M. Kelly, *Earthquake-Resistant Design with Rubber*, 2nd ed., Springer-Verlag London Limited **1997**, <https://doi.org/10.1007/978-1-4471-0971-6>.

- [2] O. Salomon, S. Oller, A. Barbat, J. *Numer. Methods Eng.* **1999**, 46, 1741.
- [3] BS EN 15129:2018 Anti-seismic devices.
- [4] P. Castillo Ruano, A. Strauss, *J. Compos. Sci.* **2021**, 5, 170.
- [5] T. Van Ngo, A. Dutta, S. K. Deb, *Earthquake Eng. Struct. Dyn.* **2017**, 46, 1747.
- [6] A. Strauss, E. Apostolidi, T. Zimmermann, U. Gerhafer, S. Dritsos, *Eng. Struct.* **2014**, 75, 402.
- [7] H. Sheikh, R. Ruparathna, Van Engelen, *Eng. Struct.* **2022**, 251, 113500.
- [8] N. Stratton, J. Cercel, S. Sinjari, N. C. Van Engelen, in *Proc. Canadian Society of Civil Engineering Annual Conf.*, Springer Nature, Singapore **2021**.
- [9] N. C. Van Engelen, M. J. Tait, D. Konstantinidis, in *Proc. 10th National Conf. Earthquake Engineering*, Anchorage, Alaska **2014**.
- [10] E. Tubaldi, S. A. Mitoulis, H. Ahmadi, *Soil Dyn. Earthquake Eng.* **2017**, 104, 329.
- [11] A. R. Bhuiyan, Y. Okui, H. Mitamura, T. Imai, *Int. J. Solids Struct.* **2009**, 46, 1778.
- [12] A. H. Deringöl, E. M. Güneyisi, *Int. J. Steel Struct.* **2021**, 21, 1698.
- [13] N. D. Oliveto, A. A. Markou, A. Athanasiou, *Soil Dyn. Earthquake* **2019**, 118, 179.
- [14] X. Zhou, L. Wang, X. Cao, Q. Yin, G. Weng, *J. Appl. Polym. Sci.* **2019**, 136, 47278.
- [15] H. Li, L. Yang, G. Weng, W. Xing, J. Wu, G. Huang, *J. Mater. Chem. A* **2015**, 3, 22385.
- [16] M. Hernández, M. del Mar Bernal, R. Verdejo, T. A. Ezquerra, M. A. Lopez-Manchado, *Compos. Sci. Technol.* **2012**, 73, 40.
- [17] X. Liu, W. Kuang, B. Guo, *Polymer* **2015**, 56, 553.
- [18] M. R. Marsico, J. M. Londoño Monsalve, D. W. Shin, M. F. Craciun, *Adv. Eng. Mater.* **2020**, 22, 1900852.
- [19] D. W. Shin, M. D. Barnes, K. Walsh, D. Dimov, P. Tian, A. I. S. Neves, C. D. Wright, S. M. Yu, J. B. Yoo, S. Russo, M. F. Craciun, *Adv. Mater.* **2018**, 30, 1802953.
- [20] F. Aziz, A. F. Ismail, *Mater. Sci. Semicond. Process.* **2015**, 39, 416.
- [21] A. T. Barrows, A. J. Pearson, C. K. Kwak, A. D. F. Dunbar, A. R. Buckley, D. G. Lidzey, *Energy Environ. Sci.* **2014**, 7, 2944.
- [22] S. Liu, X. Zhang, L. Zhang, *Sci. Rep.* **2016**, 6, 37042.
- [23] J. G. Tait, B. J. Worfolk, S. A. Maloney, T. C. Hauger, A. L. Elias, J. M. Buriak, K. D. Harris, *Sol. Energy Mater. Sol. Cells* **2013**, 110, 98.
- [24] R. C. Tenent, T. M. Barnes, J. D. Bergeson, A. J. Ferguson, B. To, L. M. Gedvilas, M. J. Heben, J. L. Blackburn, *Adv. Mater.* **2009**, 21, 3210.
- [25] J. Stryckers, T. Swusten, W. Brullot, J. D'Haen, T. Verbiest, W. Deferme, *Adv. Eng. Mater.* **2018**, 20, 1800681.
- [26] ISO 37, *Rubber, Vulcanized or Thermoplastic - Determination of Tensile Stress-Strain Properties*, ISO copyright office, Geneva, Switzerland **2017**.
- [27] ASTM 2019 section 9 Rubber.
- [28] J. T. Bauman, *Fatigue, Stress and Strain of Rubber Components - Guide for Design Engineer*, Hanser, Munich, Germany **2008**.
- [29] P. B. Lindley, *Engineering Design with Natural Rubber*, Malaysian Rubber Producers' Research Association, Tun Abdul Razak Laboratory, Brickendonbury, Hertford **1981**.
- [30] R. J. Schaefer, *Mechanical Properties of Rubber*, In *Harris' Shock and Vibration Handbook*, The McGraw-Hill Companies, Inc. **2001**, Ch. 33, ISBN 0-07-137081-1.
- [31] ISO 48-6, *Apparent Hardness of Rubber-Covered Rollers by IRHD Method*, ISO copyright office, Geneva, Switzerland **2018**.
- [32] F. Naeim, J. M. Kelly, *Design of Seismic Isolated Structures from Theory to Practice*, John Wiley & Sons. Inc., New York, NY **1999**.
- [33] A. N. Gent, *Engineering with Rubber - How to Design Rubber Components*, Hanser, Munich, Germany **2012**, Ch. 3.
- [34] P. B. Lindley, *Engineering Design with Natural Rubber*, N.Z. Technical Bull., Malaysian Rubber Producers Research Association, Brickendonbury, Hertford **1960**.
- [35] A. N. Gent, *Rubber Chem. Technol.* **1958**, 31, 896.
- [36] BS 903, *Methods of Testing Vulcanised Rubber Part 19*, BSI, London **1950**, p. 114, and Part A7, 1957.
- [37] I. M. Meththananda, S. Parker, M. P. Patel, M. Braden, *Dental Mater.* **2009**, 25, 956.
- [38] A. E. H. Love, *The Mathematical Theory of Elasticity*, 4th ed., Cambridge University Press, Cambridge **1927**.
- [39] BS 903, *A26 Method for Determination of Hardness (Hardness between 10 IRHD and 100 IRHD)*, BS 903, A26:1995, International Organization for Standardization, Geneva, Switzerland **1995**.
- [40] S. Nasrazadani, S. Hassani, in *Handbook of Materials Failure Analysis with Case Studies from the Oil and Gas Industry* (Eds: A. S. Hamdy Makhoulouf, M. Aliofkhaezraei), Butterworth-Heinemann, Elsevier, **2015**, pp. 39–54, Ch. 2, ISBN 9780081001172.
- [41] K. N. Kalfas, S. A. Mitoulis, D. Konstantinidis, *J. Struct. Eng.* **2020**, 146, 10.
- [42] R. G. Tyler, *Bull. N. Z. Soc. Earthq. Eng.* **1991**, 24, 3.
- [43] A. Dorfmann, R. W. Ogden, *Int. J. Solids Struct.* **2004**, 41, 1855.
- [44] R. W. Ogden, D. G. Roxburgh, *Proc. R. Soc. Lond. A* **1999**, 455, 2861.
- [45] D. D. Milašinović, *Int. J. Solids Struct.* **2007**, 44, 7143.